

pubs.acs.org/JACS Article

# Atomically Precise Au<sub>42</sub> Nanorods with Longitudinal Excitons for an Intense Photothermal Effect

Yingwei Li,\*\*,\*\* Yongbo Song,\*\* Xinwen Zhang, Tongyu Liu, Tingting Xu, He Wang, De-en Jiang, and Rongchao Jin\*



Cite This: J. Am. Chem. Soc. 2022, 144, 12381-12389



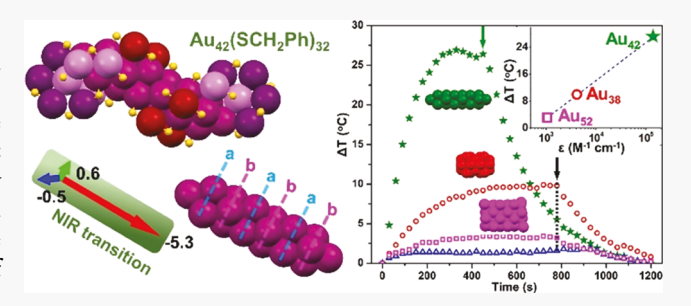
**ACCESS** 

Metrics & More

Article Recommendations

s Supporting Information

**ABSTRACT:** Metallic-state gold nanorods are well known to exhibit strong longitudinal plasmon excitations in the near-infrared region (NIR) suitable for photothermal conversion. However, when the size decreases below  $\sim$ 2 nm, Au nanostructures become nonmetallic, and whether the longitudinal excitation in plasmonic nanorods can be inherited is unknown. Here, we report atomically precise rod-shaped  ${\rm Au_{42}(SCH_2Ph)_{32}}$  with a hexagonal-close-packed  ${\rm Au_{20}}$  kernel of aspect ratio as high as 6.2, which exhibits an intense absorption at 815 nm with a high molar absorption coefficient of  $1.4 \times 10^5~{\rm M}^{-1}~{\rm cm}^{-1}$ . Compared to other rod-shaped nanoclusters,  ${\rm Au_{42}}$  possesses a much more effective photothermal conversion



with a large temperature increase of  $\sim$ 27 °C within 5 min ( $\lambda_{\rm ex}$  = 808 nm, 1 W cm<sup>-2</sup>) at an ultralow concentration of 50  $\mu \rm g$  mL<sup>-1</sup> in toluene. Density functional theory calculations show that the NIR transition is mainly along the long axis of the Au<sub>20</sub> kernel in Au<sub>42</sub>, i.e., a longitudinal excitonic oscillation, akin to the longitudinal plasmon in metallic-state nanorods. Transient absorption spectroscopy reveals that the fast decay in Au<sub>42</sub> is similar to that of shorter-aspect-ratio nanorods but is followed by an additional slow decay with a long lifetime of 2400 ns for the Au<sub>42</sub> nanorod. This work provides the first case that an intense longitudinal excitation is obtained in molecular-like nanorods, which can be used as photothermal converters and hold potential in biomedical therapy, photoacoustic imaging, and photocatalysis.

#### INTRODUCTION

In nanotechnology, gold nanoparticles provide remarkable opportunities due to their strongly enhanced optical properties associated with surface plasmon resonance (SPR). The strong SPR absorption can be efficiently converted to heat via rapid electron-phonon and phonon-phonon processes.<sup>2</sup> Due to their unique optical properties as well as low toxicity, gold nanoparticles (e.g., spheres and rods) have been used to heat up a local environment by radiation with a frequency within the SPR absorption band and are utilized in medical applications, especially in photothermal therapy and cancer diagnostics.<sup>3–8</sup> Gold nanorods with tunable longitudinal SPR in the near-infrared region (NIR) are highly desired to target malignant cells without damaging the surrounding healthy tissues. Typically, the aspect ratio (AR) of gold nanorods is tuned to ~4 to have an SPR band at ~800 nm to match the most commonly used 808 nm laser for minimum extinction by human tissues (i.e., deeper penetration). 9-11

When the dimensions of gold nanoparticles are reduced to a critical size ( $\sim$ 2 nm), a transition from metallic to nonmetallic occurs due to quantized electronic energy levels and the SPR gives way to excitons, <sup>12–15</sup> manifested in multiple discrete absorption peaks. <sup>16–18</sup> These ultrasmall nanoparticles, commonly called nanoclusters (NCs), have achieved atomic

precision and attracted much attention in recent research, with their optical, <sup>19</sup> photoluminescent, <sup>20</sup> chiral, <sup>21</sup> electronic, <sup>22</sup> and magnetic properties, <sup>23–25</sup> as well as assembly <sup>26,27</sup> and catalytic applications <sup>28,29</sup> being understood based on the fully solved structures by X-ray crystallography. However, the NCs possess no enhanced electromagnetic fields (i.e., near fields) surrounding the particle surface, especially in the NIR. The NCs with less than 50 gold atoms usually have successive absorption peaks in the visible region, and when the size increases (>100 Au atoms), a long absorption tail extends into the NIR as the energy gap becomes smaller; <sup>18</sup> in other words, the absorption intensity of NCs drastically decreases at longer wavelengths, and hence, efficient photothermal conversion is not possible by NIR excitation.

Fortunately, the structure of NCs can be tailored via atomically precise nanochemistry, <sup>19</sup> and one-dimensional (1D) nanorods are highly desired, which may generate longitudinal

Received: April 12, 2022 Published: June 29, 2022





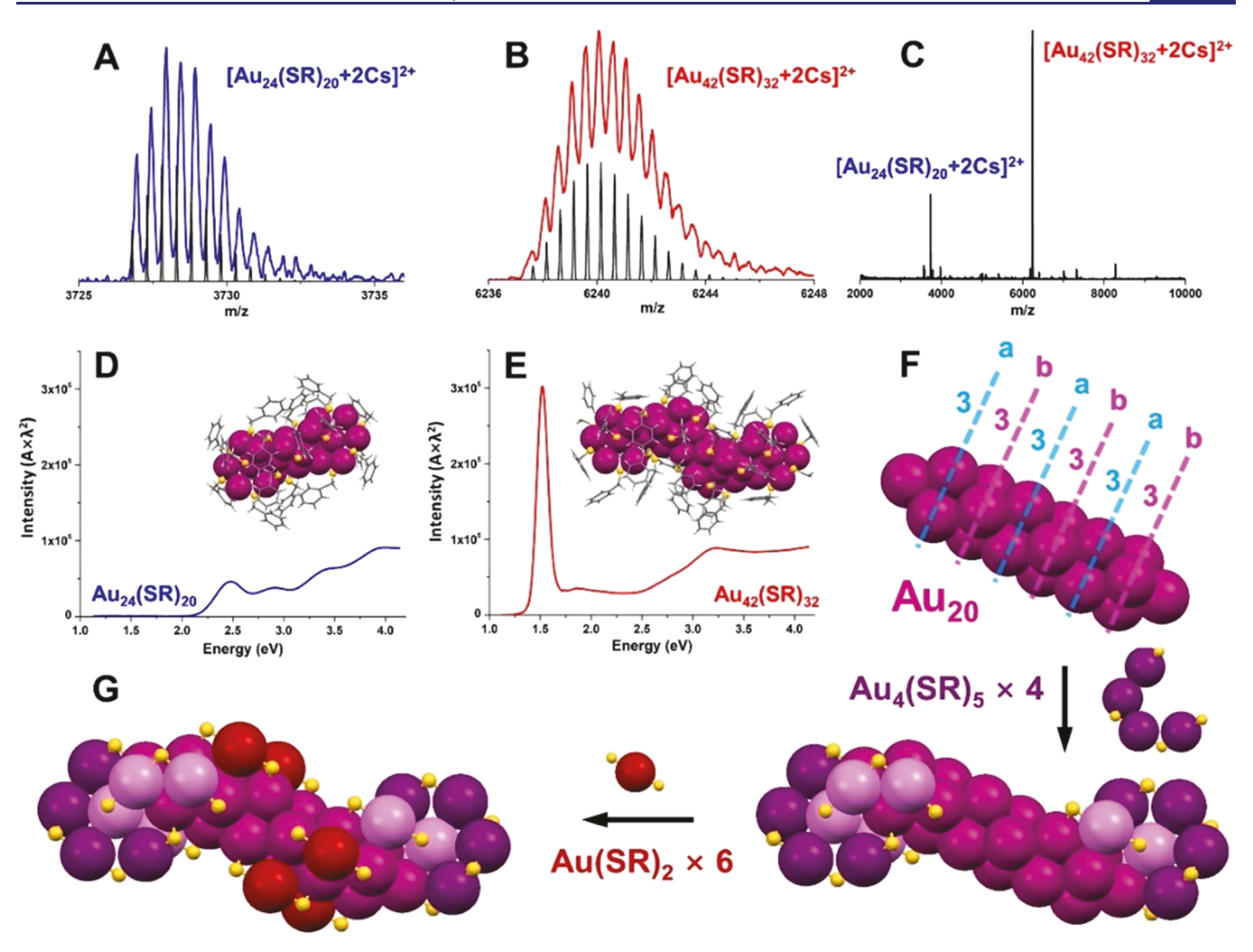


Figure 1. Isotope patterns of (A)  $[Au_{24}(SCH_2Ph)_{20} + 2Cs]^{2+}$  and (B)  $[Au_{42}(SCH_2Ph)_{32} + 2Cs]^{2+}$  in (C) the full ESI mass spectrum. CsOAc was used to impart charges by forming adducts of clusters with Cs+. Normalized absorption spectra (photon energy scale) of (D)  $Au_{24}(SCH_2Ph)_{20}$  and (E)  $Au_{42}(SCH_2Ph)_{32}$  nanorods, with corresponding structures shown in the insets, respectively. The total structure of  $Au_{24}(SCH_2Ph)_{20}$  is recreated by the authors from the data in ref 42. (F) Rod-shaped hcp  $Au_{20}$  kernel of  $Au_{42}(SR)_{32}$ . (G) Two pairs of interlocked  $Au_4(SR)_5$  staple motifs (four motifs total) protecting the two ends of the  $Au_{20}$  kernel, and six  $Au(SR)_2$  staple motifs protecting the body of the  $Au_{20}$  kernel. Color codes: magenta/violet/purple/red,  $Au_5$  yellow,  $S_5$  gray,  $C_5$  and white, H.

excitonic transitions at long wavelengths, just like what was observed in their plasmonic counterparts. Structurally characterized, atomically precise nanorods are much fewer than nanospheres due to the dramatically increased surface energy.<sup>30-33</sup> All of the ultrasmall nanorods reported so far are composed of two or more icosahedral  $M_{13}$  (M = Au/Ag/ Pt) building blocks connected via vertex sharing, and absorption in the NIR was observed. 30-33 As for NCs with face-centered-cubic (fcc) atomic structure (the same as bulk noble metals and their nanoparticles), homodimeric and heterodimeric structures can also be regarded as nanorods with small aspect ratios.<sup>27,34</sup> Periodicity in gold quantum-box NCs was observed in a series of  $Au_{8n+4}(SR)_{4n+8}$  (SR = thiolate) with integral numbers of (001) layers  $(n = 3 \text{ to } 6)^{35}$  and the magic number can go as high as n = 9 in experiments,<sup>36</sup> although only its simulated structure<sup>37</sup> (as opposed to the experimental structure) is available thus far. As the 1D structure of this fcc series becomes longer, the absorption band gradually red-shifts into the NIR, offering a means to tune the absorption peak by the aspect ratio.<sup>38</sup>

Although plasmonic Au nanorods have long been used for photothermal conversion and its mechanism has also been well explained by SPR, such an important property is yet to be explored in atomically precise metal NCs with no SPR. High efficiencies in the photothermal effect of Au NCs are particularly important for applications. We aim to design molecular-like Au nanorods with a suitable aspect ratio so as to see whether the optical properties of plasmonic Au nanorods with longitudinal excitation can be inherited even at the ultrasmall size, and furthermore, whether the NIR absorption (without SPR) of molecular-like Au nanorods is still strong enough for photothermal conversion.

Herein, we report an all-thiolate-protected Au nanorod of atomic precision, i.e.,  $Au_{42}(SCH_2Ph)_{32}$  with a hexagonal-close-packed (hcp)  $Au_{20}$  kernel of an aspect ratio of 6.2, featuring very strong absorption at 815 nm with a molar absorption coefficient of  $1.4 \times 10^5 \, \mathrm{M}^{-1} \, \mathrm{cm}^{-1}$ . The  $Au_{20}$  kernel is protected by two pairs of interlocked  $Au_4(SR)_5$  motifs on the ends and six  $Au(SR)_2$  monomers around its body. Upon 808 nm excitation, the  $Au_{42}$  nanorod solution even at a very low concentration (e.g., 50  $\mu g \, \mathrm{mL}^{-1}$  in toluene) shows an effective

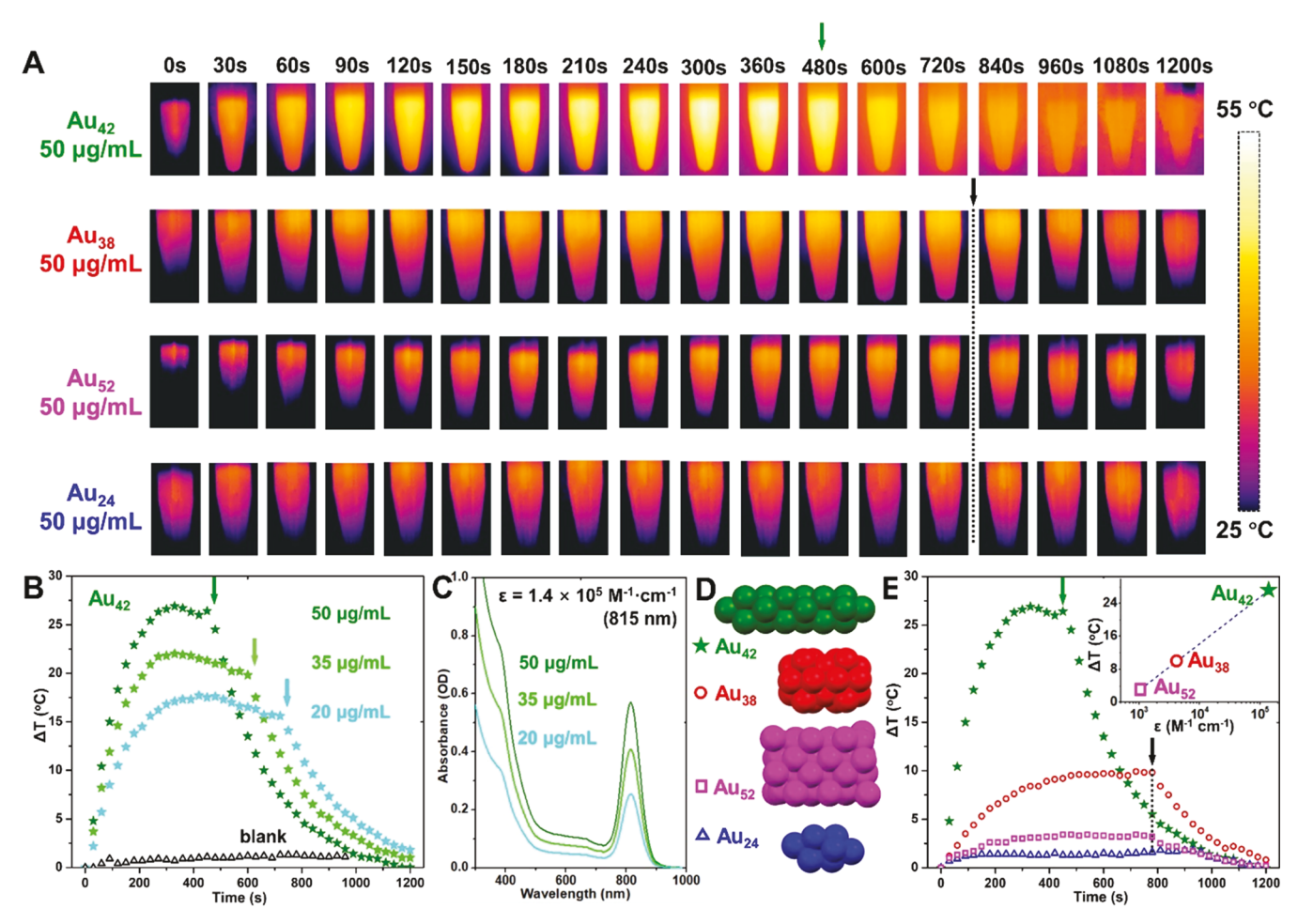


Figure 2. (A) Time-dependent images of  $Au_{42}$ ,  $Au_{38}$ ,  $Au_{52}$ , and  $Au_{24}$  solutions (50  $\mu g$  mL<sup>-1</sup>) upon laser irradiation followed by a cooling period (arrows indicate the time of stopping irradiation). (B) Temperature change of  $Au_{42}$  solutions with different concentrations (50, 35, or 20  $\mu g$  mL<sup>-1</sup>), and (C) the corresponding absorption spectra of the  $Au_{42}$  solutions. (D) Kernel structures of  $Au_{42}$ ,  $Au_{38}$ ,  $Au_{52}$ , and  $Au_{24}$  nanorods. (E) Temperature change of  $Au_{42}$ ,  $Au_{38}$ ,  $Au_{52}$ , and  $Au_{24}$  solutions (50  $\mu g$  mL<sup>-1</sup>), inset: the relationship between temperature change and molar absorption coefficient of NC solutions at irradiation wavelength. Solvent: toluene. Laser irradiation: 808 nm, 1 W cm<sup>-2</sup>. Arrows indicate the time to stop the irradiation.

photothermal conversion (e.g., a temperature increase by ~27 °C within 5 min). Based on the X-ray structure, timedependent density functional theory (TDDFT) simulations clearly indicate that the NIR peak of Au<sub>42</sub> corresponds to an electronic transition along the long axis of the Au<sub>20</sub> kernel, i.e., a longitudinal exciton excitation. The strong photothermal conversion is ascribed to the confinement of excitons inside the rod-shaped kernel. Transient absorption analyses show that, in addition to a fast decay (<1 ps), the Au<sub>42</sub> nanorod has a slow decay in the NIR, with its long lifetime of 2400 ns. The present work demonstrates that the longitudinal excitation of plasmonic Au nanorods can be inherited by atomically precise ultrasmall nanorods with exciton states below the size of 2 nm, and although there is no SPR, the NIR excitonic absorption can be very intense and lead to strong photothermal conversion.

#### RESULTS AND DISCUSSION

Synthesis and Characterization of  $Au_{42}(SCH_2Ph)_{32}$  Nanorods. A mild reducing agent, borane tert-butylamine complex  $(C_4H_9NH_2\cdot BH_3)$ , was used to reduce the  $[Au^I(SCH_2Ph)]_x$  precursor. Dark NCs were observed in a short time, and the reaction was kept overnight under ambient

conditions. The crude product was obtained by rotary evaporation of the solvent and thorough washing with methanol. The mixture of Au NCs was then extracted with CH<sub>2</sub>Cl<sub>2</sub> and concentrated for thin-layer chromatography (TLC) separation (see the Supporting Information for details). Four different bands (Figure S1A) were identified at the top of the plate according to their different UV-vis absorption spectra, including the first light brown band of Au<sub>25</sub>(SCH<sub>2</sub>Ph)<sub>18</sub>, the second dark brown band of Au<sub>38</sub>(SCH<sub>2</sub>Ph)<sub>24</sub>, the third orange band of Au<sub>24</sub>(SCH<sub>2</sub>Ph)<sub>20</sub>, and the fourth green band that was characterized to be a novel Au<sub>42</sub>(SCH<sub>2</sub>Ph)<sub>32</sub> product. Au<sub>24</sub>(SCH<sub>2</sub>Ph)<sub>20</sub> shows an orange color of fluorescence under UV light (Figure S1B), which is consistent with the literature. 42 Au<sub>25</sub>(SCH<sub>2</sub>Ph)<sub>18</sub> and Au<sub>38</sub>(SCH<sub>2</sub>Ph)<sub>24</sub> are first reported, and their absorption profiles are almost identical to those of the structure-solved  $Au_{25}(SC_2H_4Ph)_{18}$  and  $Au_{38}(SC_2H_4Ph)_{24}$  with one  $-CH_2$ difference in the thiolates (Figure S2A/B). 16,43 The structure of  $Au_{24}(SCH_2Ph)_{20}$  is relevant to that of  $Au_{24}(SCH_2Ph^{-t}Bu)_{20}$ with the latter ligand bearing an additional tert-butyl group, and the two NCs also show very similar absorption spectra (Figure S2C). 42,44

Electrospray ionization (ESI) mass spectrometry was employed to determine the formulas of NCs. As the experimental isotopic patterns of [Au<sub>24</sub>(SCH<sub>2</sub>Ph)<sub>20</sub>+2Cs]<sup>2+</sup> and [Au<sub>42</sub>(SCH<sub>2</sub>Ph)<sub>32</sub>+2Cs]<sup>2+</sup> (Figure 1A/B, blue/red lines) match well with the calculated ones (Figure 1A/B, black lines), the formulas of the two NCs are confirmed. The full ESI mass spectrum (Figure 1C) shows that residual Au<sub>24</sub>(SR)<sub>40</sub> NCs are mixed with Au<sub>42</sub>(SR)<sub>32</sub> in the raw product after TLC separation, but pure Au<sub>42</sub>(SR)<sub>32</sub> can be obtained after crystallization.

In the optical absorption spectra of Au<sub>24</sub>(SR)<sub>20</sub> and  $Au_{42}(SCH_2Ph)_{32}$  (normalized at  $\lambda = 300$  nm), the lowestenergy absorption peak of Au<sub>24</sub>(SR)<sub>20</sub> is at 2.5 eV (Figure 1D). Surprisingly, the lowest-energy absorption peak for the novel Au<sub>42</sub>(SR)<sub>32</sub> red-shifts to 1.5 eV (Figure 1E) and its intensity is as strong as 6.5 times that of  $Au_{24}(SR)_{20}$ .

Previous work reported the fusion of  $Au_{25}(SR)_{18}$  into  $Au_{38}(SR)_{24^{\prime}}{}^{45}$  as well as the dimerization of two icosahedral  $M@Au_{12}$  (M = Pd/Pt) superatoms.<sup>46</sup> Since the pair of Au<sub>25</sub>(SR)<sub>18</sub> and Au<sub>38</sub>(SR)<sub>24</sub> NCs with related structures is prepared together with the pair of Au<sub>24</sub>(SR)<sub>20</sub> and Au<sub>42</sub>(SR)<sub>32</sub> NCs, one can easily relate the latter two NCs by comparing their structures (Figure 1D/E insets) as  $Au_{42}(SR)_{32}$  looks like a combination of two of  $Au_{24}(SR)_{20}$ .

A close look at the structure of Au<sub>42</sub>(SR)<sub>32</sub> reveals a rodshaped hcp kernel of an unprecedently high aspect ratio (Figure 1F and Table S1). The Au<sub>20</sub> kernel comprises six layers in an a-b-a-b-a-b manner with two Au atoms capping the two ends (i.e.,  $Au_1-Au_3-Au_3-Au_3-Au_3-Au_3-Au_3-Au_1$ ). Note that among all solved atomically precise Au NCs, there is so far only one case with hcp kernel—Au<sub>30</sub>(SR)<sub>18</sub> (i.e., Au<sub>18</sub> kernel with a Au<sub>3</sub>-Au<sub>6</sub>-Au<sub>6</sub>-Au<sub>3</sub> configuration),<sup>47</sup> which gives rise to special exciton behavior compared to NCs of other structures. 48 At the two ends of the Au<sub>20</sub> kernel, a pair of Au<sub>4</sub>(SR)<sub>5</sub> staple motifs is attached via bidentate bonding (Figure 1G, marked in violet); another pair of tetrameric staple motifs form bonds in a way, which rotates by  $\sim 90^{\circ}$  relative to the first pair (Figure 1G, marked in purple), i.e., the two Au<sub>4</sub>(SR)<sub>5</sub> motifs at the same end interlock with each other. The body of the long rod-shaped Au<sub>20</sub> kernel is further protected by six monomeric Au(SR)<sub>2</sub> motifs (Figure 1G, marked in red). In the structure of  $Au_{24}(SR)_{20}$ , the prolate  $Au_8$ kernel (Figure S3A, Au<sub>1</sub>-Au<sub>3</sub>-Au<sub>3</sub>-Au<sub>1</sub>) can be considered as a shortened form compared to the  $Au_{20}$  kernel in  $Au_{42}(SR)_{32}$ (Figure S3B). The  $Au_8$  kernel in  $Au_{24}(SR)_{20}$  is also protected by two pairs of interlocked Au<sub>4</sub>(SR)<sub>5</sub> staple motifs (Figure S3A, marked in violet/purple); however, as the kernel is much shorter, there is no more open area for other motifs. The clear relationship between the two structures reveals that  $Au_{42}(SR)_{32}$ is an elongated structure of Au<sub>24</sub>(SR)<sub>20</sub> along the long axis of the kernel.

Here, we further compare the aspect ratios of rod-shaped kernels of some reported NCs of atomic precision. As shown in Figure S4, in the kernel of  $Au_{38}(SR)_{24}^{17}$  two icosahedral  $Au_{13}$ units fuse at a common Au<sub>3</sub> facet, and the aspect ratio (AR) of the Au<sub>23</sub> kernel is only 1.8. As for the rod-shaped Au<sub>25</sub>(SR)<sub>5</sub>(PPh<sub>3</sub>)<sub>10</sub>Cl<sub>2</sub>, the two icosahedral Au<sub>13</sub> units share a vertex and the AR increases to 2.3.30 As expected, when three or four icosahedral Au<sub>13</sub> or Ag<sub>13</sub> units are linearly attached via vertex sharing, AR increases to 3.5 and 4.6, respectively. 31,33 On the other hand, although the AR of the  $Au_8$  kernel in  $Au_{24}(SR)_{20}$  is only 2.6, the AR of hcp  $Au_{20}$  kernel is 6.2 (Figure S4), which is so far the largest AR observed in atomically

precise NCs. Thus, the Au<sub>42</sub>(SR)<sub>32</sub> nanorod provides a great opportunity to study potentially new properties based on its special shape, and the confinement of excitons within the long but narrow kernel would lead to strong photothermal conversion upon photoexcitation.

Ultrasmall Au Nanorods as Photothermal Converters. To measure the photothermal conversion of  $Au_{42}(SR)_{32}$ , the NCs were dissolved in toluene (50  $\mu$ g mL<sup>-1</sup>). Figure 2A (top) shows the time-dependent images of the solution with 808 nm laser irradiation at 1 W cm<sup>-2</sup>. Interestingly, very rapid heating was observed upon excitation, as the temperature change reached ~27 °C within only ~5 min (Figure S5, Supporting Information Video, note: 4 times the actual speed). Upon removal of the NIR irradiation at the 6th min, the solution was cooled to the background temperature within ~12 min (Figure 2B, olive star), and the cooling of the toluene solution follows Newton's law,

$$T(t) = T_0 e^{-kt} + T_{\text{ambient}}$$

with the cooling constant k determined to be 0.005 s<sup>-1</sup>. The photothermal performance of the ultrasmall Au<sub>42</sub> nanorods indeed rivals the plasmonic Au nanorods with aspect ratio ~4 in phosphate-buffered saline, 49 although we deduce that the plasmonic nanorods have a k of  $\sim 0.014 \text{ s}^{-1}$  from the reported data. It should be noted that the heat capacity of toluene is 2.6 times lower than water, and the atomically precise nanorods are only organic soluble, which requires ligand modification or micelle encapsulation for future biological applications. Nevertheless, the photothermal conversion of Au<sub>42</sub> nanorods is impressive considering the very low concentration (50  $\mu$ g mL<sup>-1</sup>). Various polymer systems have been used to transfer nanoparticles from the organic phase to water without changing their physical properties, \$50,51 and we expect them to be applicable to our atomically precise nanorods as well, but this is beyond the scope of this work.

The high photothermal conversion of the Au<sub>42</sub> nanorod is related to its strong absorption in the NIR (Figure 2C). Tsukuda et al. reported a series of glutathione-protected gold NCs of atomic precision, finding that the molar absorption coefficient  $\varepsilon$  for the first (i.e., lowest-energy) peak of different Au, NCs are from  $8.5 \times 10^3$  to  $1.5 \times 10^4$  M<sup>-1</sup> cm<sup>-1</sup>  $^{52}$  Their later work on Au<sub>76</sub>(SR)<sub>44</sub> NCs showed an intense NIR band at 1340 nm with  $\varepsilon=3\times10^5~\text{M}^{-1}~\text{cm}^{-1},^{34}$  but the structure is unknown yet and no photothermal property has been reported. As for the Ag<sub>61</sub> NC containing four vertex-sharing icosahedral Ag<sub>13</sub> units, the absorption coefficient is  $6.2 \times 10^4 \, \mathrm{M}^{-1} \, \mathrm{cm}^{-1}$  at 819 nm, and this NIR absorption was ascribed to the strong electronic coupling between the silver units,<sup>33</sup> which is stronger than that between Au<sub>13</sub> units in the linear-shaped nanorod. 53 By contrast, the kernel atoms in the Au<sub>42</sub> nanorod are closely packed, and the absorption coefficient  $\varepsilon$  of  $\mathrm{Au}_{42}$  is determined to be  $1.4 \times 10^5 \,\mathrm{M}^{-1} \,\mathrm{cm}^{-1}$  at 815 nm (determined by experimental absorption according to Beer's law,  $A = \varepsilon cl$ , wherein A = 0.57 OD,  $c = 50 \,\mu\text{g mL}^{-1}/12215.15 \,\text{g mol}^{-1}$ , and l= 1 cm). The obtained absorption coefficient is indeed a very high value due to the large aspect ratio of the rod-shaped kernel, of which the origin can be further explained by TDDFT calculations (see the next section).

The Au<sub>42</sub> nanorods were also measured at different concentrations for photothermal conversion (Figure S6/S7/ S8), indicating a monotonic enhancement of the photothermal effect as a function of the nanorod concentration (Figure 2B/ C). When the concentration decreased to 35 and 20  $\mu$ g mL<sup>-1</sup>,

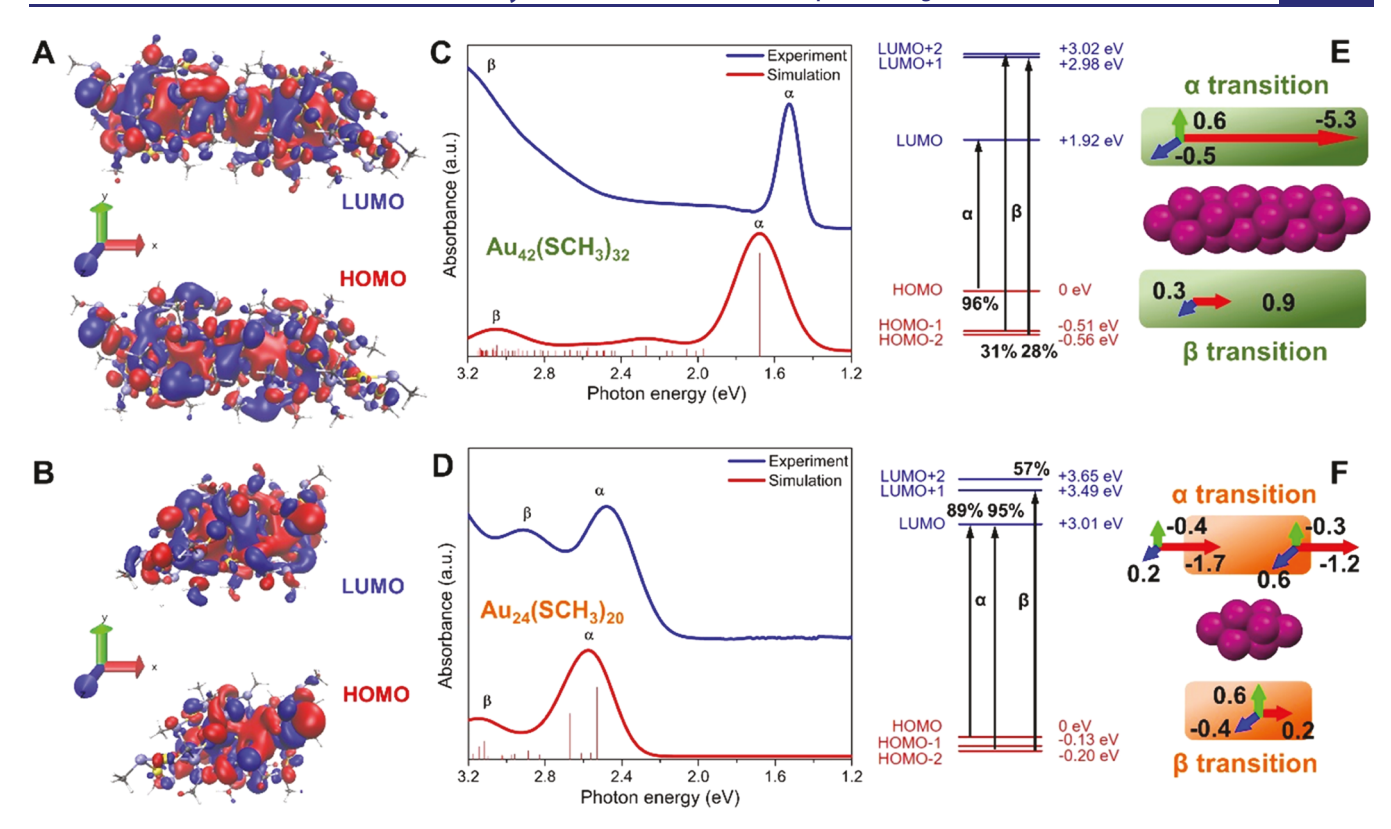


Figure 3. HOMO and LUMO orbitals of (A)  $Au_{42}(SCH_3)_{32}$  and (B)  $Au_{24}(SCH_3)_{20}$  NCs. (C) Experimental absorption spectrum of  $Au_{42}(SCH_2Ph)_{32}$  (blue line) and TDDFT-simulated absorption spectrum of  $Au_{42}(SCH_3)_{32}$  (red line), and corresponding KS orbital energy level diagram. (D) Experimental absorption spectrum of  $Au_{24}(SCH_2Ph)_{20}$  (blue line) and TDDFT-simulated absorption spectrum of  $Au_{24}(SCH_3)_{20}$  (red line), and corresponding KS orbital energy level diagram. Schematic illustrations of α and β electronic transitions for (E)  $Au_{42}(SCH_3)_{32}$  and (F)  $Au_{24}(SCH_3)_{20}$ .

although the temperature increasements were reduced to ~22 and ~17 °C, respectively, the time to reach the largest increment was similar (i.e., at ~300 s). The decline in temperature after 300 s of NIR irradiation for the 50 and 35  $\mu g$  mL<sup>-1</sup> solutions indicates partial degradation of the Au<sub>42</sub> nanorods. However, the 20  $\mu g$  mL<sup>-1</sup> solution does not show any obvious decomposition due to less heat generation (even after continuous irradiation for 10 min) based on the absorption spectroscopy analysis, and the Au<sub>42</sub> nanorods are also stable in ambient solution (Figure S9).

We also measured the photothermal conversion of other allthiol-protected Au NCs with rod-shaped kernel structures (Figure S10/S11/S12), including the Au<sub>38</sub>(SR)<sub>24</sub> with a facefused bi-icosahedral Au<sub>23</sub> kernel, Au<sub>52</sub>(SR)<sub>32</sub> with a layer-bylayer fcc kernel, and Au<sub>24</sub>(SR)<sub>20</sub> with a bi-tetrahedral Au<sub>8</sub> kernel (Figure 2D). The optical properties of these Au NCs are shown in Figure S13. At the common concentration of 50  $\mu$ g  $mL^{-1}$ , the molar absorption coefficient  $\varepsilon$  of Au<sub>38</sub> at 745 nm is  $6.7 \times 10^3 \,\mathrm{M}^{-1} \,\mathrm{cm}^{-1}$ , while that of Au<sub>52</sub> at 790 nm is quite low  $(1.1 \times 10^3 \text{ M}^{-1} \text{ cm}^{-1})$ . Correspondingly, 808 nm excitation also shows photothermal conversion by Au<sub>38</sub> (Figure 2E, red open circle) and Au<sub>52</sub> (Figure 2E, magenta open square) with temperature increases by ~10 and ~3 °C, respectively. As for Au<sub>24</sub>, it does not show any absorption in the NIR, thus only a small temperature fluctuation was observed (Figure 2E, blue open triangle) upon NIR excitation, similar to that by the blank, i.e., solvent only (Figure 2B, black open triangle). Furthermore, it is clear that the temperature increase is almost linear with respect to the exponential scale of the molar absorption coefficient at the irradiation wavelength (Figure 2E,

inset), indicating that the photothermal conversion by nonmetallic Au NCs is exponentially related to the photon absorption.

On the Nature of the NIR Transition in Atomically Precise Au Nanorods. Compared to Au nanospheres with a plasmonic maximum at  $\sim$ 520 nm, the SPR of Au nanorods splits into a relatively weak band (transverse mode of collective electron oscillation) in the visible region and a much stronger longer-wavelength band (longitudinal oscillation of conduction electrons) of which the position can be tuned by controlling the aspect ratio of the plasmonic nanorods. At ultrasmall sizes (below  $\sim$ 2 nm), nanorods of high aspect ratios are very rare; thus, we wonder whether the nonplasmonic  $Au_{42}(SR)_{32}$  rod would have a longitudinal excitation akin to the plasmonic counterpart.

DFT and TDDFT calculations  $^{54,55}$  were used here to simulate the electronic structure and optical spectra of  $Au_{42}(SCH_2Ph)_{32}$  and  $Au_{24}(SCH_2Ph)_{20}$  nanorods. The visualized orbitals (Figure 3A/B) indicate that the highest occupied molecular orbital (HOMO) and the lowest unoccupied molecular orbital (LUMO) of both  $Au_{42}$  and  $Au_{24}$  NCs are mainly localized on the  $Au_{20}$  and  $Au_{8}$  kernel, respectively, and the hcp  $Au_{20}$  kernel can be regarded as an elongation along the  $\alpha$  axis. The experimental and TDDFT-simulated absorption spectra match well with each other (Figure 3C/D, left), and the Kohn–Sham (KS) orbital diagram is used to illustrate the electronic transitions from occupied orbitals to unoccupied ones corresponding to the absorption peaks (Figure 3C/D, right), which is explained in detail below for the two NCs.

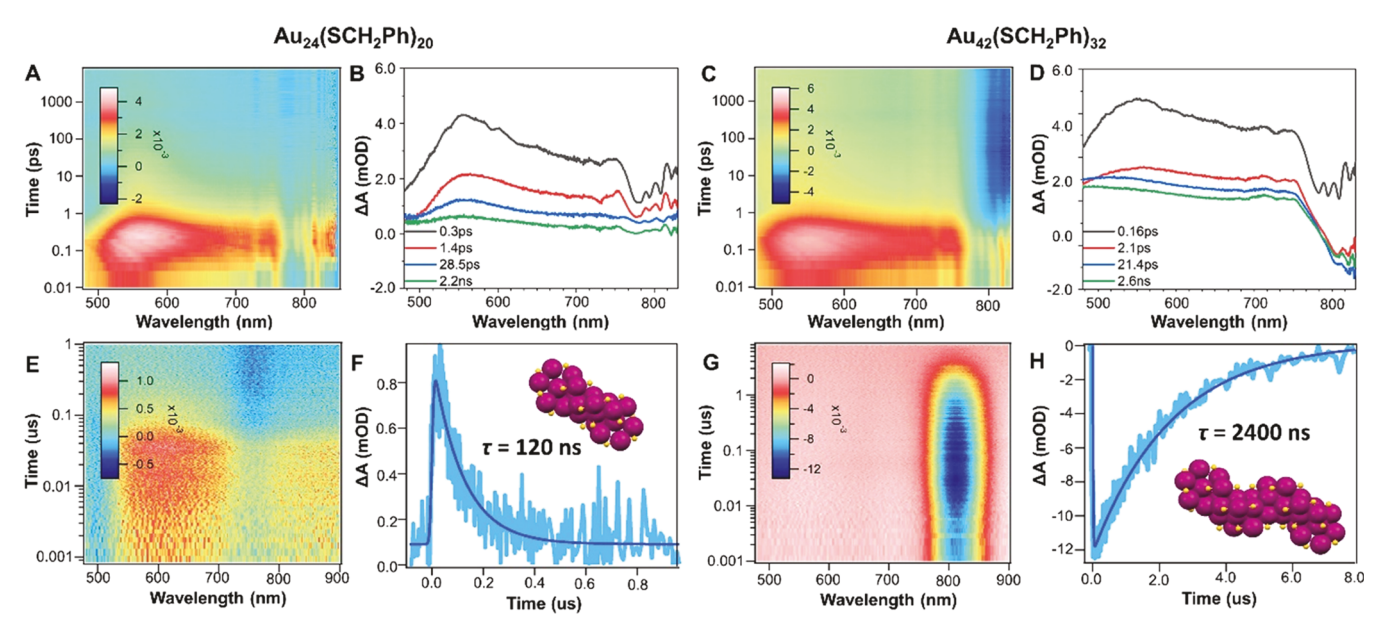


Figure 4. (A) fs-TA data map of  $Au_{24}(SCH_2Ph)_{20}$  and (B) its TA spectra at selected time delays. (C) fs-TA data map of  $Au_{42}(SCH_2Ph)_{32}$  and (D) its TA spectra at selected time delays. (E) ns-TA data map of  $Au_{24}(SCH_2Ph)_{20}$  and (F) its TA kinetic traces and fitting (probed at 580 nm). (G) ns-TA data map of  $Au_{42}(SCH_2Ph)_{32}$  and (H) its TA kinetic traces and fitting (probed at 813 nm).  $λ_{ex}$  = 400 nm; ΔA, change in absorbance (millioptical-density, mOD).

As for  $Au_{42}(SCH_3)_{32}$ , its first peak at 1.68 eV (peak  $\alpha$ ) is due to the HOMO to LUMO transition (96%) and peak  $\beta$  at much higher energy (3.05 eV) is contributed by HOMO  $-1 \rightarrow$ LUMO + 2 and HOMO  $-2 \rightarrow \text{LUMO} + 1$  transitions (Figure 3C, right). As the oscillator strength of the HOMO  $\rightarrow$  LUMO transition is much larger than the combination of HOMO - 1 $\rightarrow$  LUMO + 2 and HOMO - 2  $\rightarrow$  LUMO + 1 transitions, a much more intense absorption in the NIR results. The oscillator strength is in direct proportion to the transition energy and square of the transition dipole moment. Interestingly, the transition dipole moment of peak  $\alpha$  is much stronger along the x axis, almost 10 times those along the y and z axes (Figure 3E and Table S2), which means that the HOMO -> LUMO transition mainly occurs on the long axis of the  $Au_{20}$  kernel. In other words, the peak  $\alpha$  transition corresponding to the strong absorption in the NIR is a longitudinal transition, reminiscent of the NIR band of plasmonic Au nanorods. It is a surprise to see that even for NCs with molecular states, longitudinal excitation can be observed and is responsible for the strong absorption in the NIR. By contrast, the  $\beta$  transition does not show any preferred orientation of oscillation.

In the case of  $Au_{24}(SCH_3)_{20}$  with a kernel of a much smaller aspect ratio, its peak  $\alpha$  at 2.6 eV is due to a combination of HOMO to LUMO transition (2.53 eV, 89%) and HOMO – 2 to LUMO transition (2.67 eV, 95%), whereas peak  $\beta$  at 3.12 eV results from the HOMO – 2  $\rightarrow$  LUMO + 1 transition (Figure 3D, right). As for peak  $\alpha$  of  $Au_{24}(SCH_3)_{20}$ , although the dipole moments for both 2.53 and 2.67 eV transitions along  $\alpha$  are stronger than in the other two directions, their absolute values are obviously weaker than what is found for peak  $\alpha$  of  $Au_{42}(SCH_3)_{32}$ , corresponding to a shorter aspect ratio of the  $Au_{24}$  nanorod (Figure 3F, top). Peak  $\beta$  of  $Au_{24}(SCH_3)_{20}$  does not show any directional preference in electronic transition (Figure 3F, bottom). It is worth pointing out that, unlike the hcp  $Au_{42}$ , other molecular-like Au nanorods (e.g.,  $Au_{44}$  and  $Au_{52}$ ) of similar sizes with fcc kernels (the same

structure as plasmonic Au nanorods) do not show intense NIR absorption. Thus, the  $Au_{42}$  rod nanocluster is quite interesting in giving rise to the intense NIR absorption and also the intense photothermal effect. Based on the structural relationship between  $Au_{24}(SCH_2Ph)_{20}$  and  $Au_{42}(SCH_2Ph)_{20}$ , we believe that the hcp rod structure is likely tunable to control the position of the longitudinal excitonic excitation.

Photoexcited Electron Dynamics of Atomically Precise Au Nanorods. Due to the related structures of  $Au_{24}(SCH_2Ph)_{20}$  and  $Au_{42}(SCH_2Ph)_{32}$ , we expect their electronic properties to be related as well, so femtosecond transient absorption (fs-TA) spectroscopic analysis (pumped at 400 nm and probed between 460 and 830 nm) was performed to probe the excited-state dynamics of both nanorods. Upon photoexcitation, a broad excited-state absorption (ESA) from 550 to 750 nm is observed for Au<sub>24</sub>(SCH<sub>2</sub>Ph)<sub>20</sub> as well as two dips (ground-state bleaching, GSB) at ~500 and ~780 nm (Figure 4A/B), consistent with the result on  $Au_{24}(SCH_2Ph^{-t}Bu)_{20}$  (with the  $-^{t}Bu$  difference) reported before. 18 A rapid decay of the ESA band is observed just after 1 ps, and the exciton decays to the ground state within 2 ns. The longer nanorod, Au<sub>42</sub>(SCH<sub>2</sub>Ph)<sub>32</sub>, shows very similar ESA immediately upon excitation (Figures 4C/D and S14A/B). Global fitting of ESA from 480 to 770 nm shows two short components (0.8 ps, 71% and 55 ps, 16%) as well as a long component (23 ns, 13%) for Au<sub>24</sub> (Figure S14C), whereas global fitting of Au<sub>42</sub> from 480 to 730 nm is also composed of three components (Figure S14D), including two short ones of 0.7 ps (78%) and 69 ps (11%) and a long component of 34 ns (11%). The close similarity in fast decay can be ascribed to the related structures<sup>56</sup> from the kernel to surface motifs of the two Au nanorods. Distinctively, the Au<sub>42</sub> nanorod has an additional GSB centered at 820 nm, which appears within 2 ps and remains almost unchanged between 2 and 7000 ps (Figure 4C/D). The fs-TA kinetic traces and fitting at 813 nm indicate a much longer lifetime, which is beyond the scope of femtosecond measurement (Figure S14E).

To probe the longer components, nanosecond-TA ( $\lambda_{ex}$  = 400 nm) was used to obtain the complete excited-state lifetimes of the two nanorods. The data showed a singleexponential decay lifetime ( $\tau$ ) of 120 ns for Au<sub>24</sub> (Figure 4E/ F) and 2400 ns for Au<sub>42</sub> (Figure 4G/H). In sharp contrast to the fs-TA, the ns-TA spectra at selected time delays for the two NCs are very different. With the increase in time delay, the ESA of Au<sub>24</sub> becomes weaker and almost disappears at 30 ns (Figure S15A). However, Au<sub>42</sub> shows a strong and long-lived GSB at ~813 nm, which becomes even stronger from 3 to 30 ns (a rise period), and then, the GSB begins to decay during a very long period of 3700 ns (Figure S15B). Of note, the other hcp NC, the  $Au_{30}(SR)_{18}$  with an hcp  $Au_{18}$  kernel, instead has a very short lifetime of 1 ns. 48 Therefore, the current Au<sub>42</sub>(SR)<sub>32</sub> (an hcp Au<sub>20</sub> kernel) shows a 2400 times longer lifetime, demonstrating that the 3-orders-of-magnitude difference in exciton recombination dynamics is related to the detailed structure of the core.

#### CONCLUSIONS

In summary, an all-thiolate-protected Au<sub>42</sub>(SCH<sub>2</sub>Ph)<sub>32</sub> nanorod with a rare hcp  $Au_{20}$  kernel is obtained and the atomic packing of Au<sub>1</sub>-Au<sub>3</sub>-Au<sub>3</sub>-Au<sub>3</sub>-Au<sub>3</sub>-Au<sub>3</sub>-Au<sub>1</sub> in the kernel shows so far the largest aspect ratio of 6.2. Due to the long rod-shaped structure, Au<sub>42</sub> demonstrates a strong absorption peak centered at 815 nm with a molar absorption coefficient as high as  $\varepsilon_{815} = 1.4 \times 10^5 \,\mathrm{M}^{-1} \,\mathrm{cm}^{-1}$ , which is close to the 808 nm laser commonly used in photothermal therapy. The photothermal conversion by  $Au_{42}$  nanorods (50  $\mu g$  m $\hat{L}^{-1}$ in toluene) is studied and a temperature increase up to  $\sim$ 27  $^{\circ}$ C is observed within only 5 min upon excitation (1 W cm<sup>-2</sup>). A comparison with other rod-shaped Au, NCs in the molecular state indicates that the temperature increment is linearly related to the exponential scale of  $\varepsilon$  at the irradiation wavelength. TDDFT simulations indicate that the electronic transition of the NIR peak of Au<sub>42</sub> is mainly along the long axis of the rod-shaped kernel, mimicking the longitudinal plasmon of metallic-state Au nanorods. Finally, transient absorption spectroscopy measurements on Au<sub>42</sub> and Au<sub>24</sub> with the same ligand and related structures (long and short nanorods) provide further insights. It is clear that, although almost the same fast decay is observed in both nanorods, Au<sub>42</sub> shows an additional very slow decay in the NIR. This work presents the first case to use atomically precise nanorods as photothermal converters, opening a new application for these emerging nanomaterials of atomic precision.

#### ASSOCIATED CONTENT

#### Supporting Information

The Supporting Information is available free of charge at https://pubs.acs.org/doi/10.1021/jacs.2c03948.

Details of synthesis, X-ray crystallography, time-dependent images of photothermal conversion, computational details, KS orbital analysis, and transient absorption spectroscopy (PDF)

Video for photothermal conversion of  $Au_{42}(SCH_2Ph)_{32}$  (MP4)

#### **Accession Codes**

CCDC 2158149 contains the supplementary crystallographic data for this paper. These data can be obtained free of charge via www.ccdc.cam.ac.uk/data\_request/cif, or by emailing data request@ccdc.cam.ac.uk, or by contacting The Cam-

bridge Crystallographic Data Centre, 12 Union Road, Cambridge CB2 1EZ, UK; fax: +44 1223 336033.

#### AUTHOR INFORMATION

#### **Corresponding Authors**

Yingwei Li — Department of Chemistry, Carnegie Mellon University, Pittsburgh, Pennsylvania 15213, United States; Present Address: Department of Chemistry and Chemical Biology, Harvard University, Cambridge, Massachusetts 02138, United States; orcid.org/0000-0002-4813-6009; Email: yingweili@fas.harvard.edu

Rongchao Jin — Department of Chemistry, Carnegie Mellon University, Pittsburgh, Pennsylvania 15213, United States; orcid.org/0000-0002-2525-8345; Email: rongchao@andrew.cmu.edu

#### Authors

Yongbo Song — School of Biomedical Engineering, Research and Engineering Center of Biomedical Materials, Anhui Medical University, Hefei, Anhui 230601, China

Xinwen Zhang — Department of Physics, University of Miami, Coral Gables, Florida 33146, United States

Tongyu Liu – Department of Chemistry, University of California, Riverside, California 92521, United States

Tingting Xu — School of Biomedical Engineering, Research and Engineering Center of Biomedical Materials, Anhui Medical University, Hefei, Anhui 230601, China

**He Wang** — Department of Physics, University of Miami, Coral Gables, Florida 33146, United States; o orcid.org/0000-0003-1365-0304

De-en Jiang — Department of Chemistry, University of California, Riverside, California 92521, United States; orcid.org/0000-0001-5167-0731

Complete contact information is available at: https://pubs.acs.org/10.1021/jacs.2c03948

#### **Author Contributions**

"Y.L. and Y.S. contributed equally to this work.

#### Notes

The authors declare no competing financial interest.

#### ACKNOWLEDGMENTS

R.J. acknowledges the NSF support (DMR 1808675). H.W. acknowledges the financial support through the Air Force Office of Scientific Research (AFOSR) Award FA9550-17-1-0099 and FA9550-21-1-0192. DFT computation (D.J.) was supported by the U.S. Department of Energy, Office of Science, Office of Basic Energy Sciences, Chemical Sciences, Geosciences, and Biosciences Division, Catalysis Science Program. Y.S. thanks for the startups.

#### REFERENCES

- (1) Murphy, C. J.; Chang, H.-H.; Falagan-Lotsch, P.; Gole, M. T.; Hofmann, D. M.; Hoang, K. N. L.; McClain, S. M.; Meyer, S. M.; Turner, J. G.; Unnikrishnan, M.; Wu, M.; Zhang, X.; Zhang, Y. Virus-Sized Gold Nanorods: Plasmonic Particles for Biology. *Acc. Chem. Res.* **2019**, *52*, 2124–2135.
- (2) Link, S.; El-Sayed, M. A. Shape and Size Dependence of Radiative, Non-Radiative and Photothermal Properties of Gold Nanocrystals. *Int. Rev. Phys. Chem.* **2000**, *19*, 409–453.
- (3) Chen, J.; Glaus, C.; Laforest, R.; Zhang, Q.; Yang, M.; Gidding, M.; Welch, M. J.; Xia, Y. Gold Nanocages as Photothermal Transducers for Cancer Treatment. *Small* **2010**, *6*, 811–817.

- (4) Moghimi, S. M.; Hunter, A. C.; Murray, J. C. Long-Circulating and Target-Specific Nanoparticles: Theory to Practice. *Pharmacol. Rev.* **2001**, *53*, 283–318.
- (5) Ferrari, M. Cancer Nanotechnology: Opportunities and Challenges. *Nat. Rev. Cancer* **2005**, *5*, 161–171.
- (6) Rosi, N. L.; Mirkin, C. A. Nanostructures in Biodiagnostics. Chem. Rev. 2005, 105, 1547–1562.
- (7) Huang, X.; Jain, P. K.; El-Sayed, I. H.; El-Sayed, M. A. Gold Nanoparticles: Interesting Optical Properties and Recent Applications in Cancer Diagnostics and Therapy. *Nanomedicine* **2007**, *2*, 681–693.
- (8) Albanese, A.; Tang, P. S.; Chan, W. C. W. The Effect of Nanoparticle Size, Shape, and Surface Chemistry on Biological Systems. *Annu. Rev. Biomed. Eng.* **2012**, *14*, 1–16.
- (9) Jiang, X.; Du, B.; Tang, S.; Hsieh, J.-T.; Zheng, J. Photoacoustic Imaging of Nanoparticle Transport in the Kidneys at High Temporal Resolution. *Angew. Chem., Int. Ed.* **2019**, *58*, 5994–6000.
- (10) Li, Z.; Huang, H.; Tang, S.; Li, Y.; Yu, X.-F.; Wang, H.; Li, P.; Sun, Z.; Zhang, H.; Liu, C.; Chu, P. K. Small Gold Nanorods Laden Macrophages for Enhanced Tumor Coverage in Photothermal Therapy. *Biomaterials* **2016**, *74*, 144–154.
- (11) Ali, M. R. K.; Rahman, M. A.; Wu, Y.; Han, T.; Peng, X.; Mackey, M. A.; Wang, D.; Shin, H. J.; Chen, Z. G.; Xiao, H.; Wu, R.; Tang, Y.; Shin, D. M.; El-Sayed, M. A. Efficacy, Long-Term Toxicity, and Mechanistic Studies of Gold Nanorods Photothermal Therapy of Cancer in Xenograft Mice. *Proc. Natl. Acad. Sci. U.S.A.* **2017**, *114*, No. E3110.
- (12) Higaki, T.; Zhou, M.; Lambright, K. J.; Kirschbaum, K.; Sfeir, M. Y.; Jin, R. Sharp Transition from Nonmetallic Au<sub>246</sub> to Metallic Au<sub>279</sub> with Nascent Surface Plasmon Resonance. *J. Am. Chem. Soc.* **2018**, *140*, 5691–5695.
- (13) Hu, F.; Guan, Z.-J.; Yang, G.; Wang, J.-Q.; Li, J.-J.; Yuan, S.-F.; Liang, G.-J.; Wang, Q.-M. Molecular Gold Nanocluster Au<sub>156</sub> Showing Metallic Electron Dynamics. *J. Am. Chem. Soc.* **2021**, 143, 17059–17067.
- (14) Takahata, R.; Yamazoe, S.; Koyasu, K.; Koyasu, K.; Imura, K.; Imura, K.; Tsukuda, T. Gold Ultrathin Nanorods with Controlled Aspect Ratios and Surface Modifications: Formation Mechanism and Localized Surface Plasmon Resonance. J. Am. Chem. Soc. 2018, 140, 6640–6647.
- (15) López-Lozano, X.; Barron, H.; Mottet, C.; Weissker, H.-C. Aspect-Ratio- and Size-Dependent Emergence of the Surface-Plasmon Resonance in Gold Nanorods—An ab initio TDDFT study. *Phys. Chem. Chem. Phys.* **2014**, *16*, 1820–1823.
- (16) Zhu, M.; Aikens, C. M.; Hollander, F. J.; Schatz, G. C.; Jin, R. Correlating the Crystal Structure of a Thiol-Protected Au<sub>25</sub> Cluster and Optical Properties. *J. Am. Chem. Soc.* **2008**, *130*, 5883–5885.
- (17) Qian, H.; Eckenhoff, W. T.; Zhu, Y.; Pintauer, T.; Jin, R. Total Structure Determination of Thiolate-Protected Au<sub>38</sub> Nanoparticles. J. Am. Chem. Soc. **2010**, 132, 8280–8281.
- (18) Zhou, M.; Higaki, T.; Li, Y.; Zeng, C.; Li, Q.; Sfeir, M. Y.; Jin, R. Three-Stage Evolution from Nonscalable to Scalable Optical Properties of Thiolate-Protected Gold Nanoclusters. *J. Am. Chem. Soc.* **2019**, *141*, 19754–19764.
- (19) Li, Y.; Zhou, M.; Jin, R. Programmable Metal Nanoclusters with Atomic Precision. *Adv. Mater.* **2021**, *33*, No. 2006591.
- (20) Kang, X.; Zhu, M. Tailoring the Photoluminescence of Atomically Precise Nanoclusters. *Chem. Soc. Rev.* **2019**, *48*, 2422–2457.
- (21) Li, Y.; Higaki, T.; Du, X.; Jin, R. Chirality and Surface Bonding Correlation in Atomically Precise Metal Nanoclusters. *Adv. Mater.* **2020**, *32*, No. 1905488.
- (22) Yuan, P.; Zhang, R.; Selenius, E.; Ruan, P.; Yao, Y.; Zhou, Y.; Malola, S.; Häkkinen, H.; Teo, B. K.; Cao, Y.; Zheng, N. Solvent-Mediated Assembly of Atom-Precise Gold—Silver Nanoclusters to Semiconducting One-Dimensional Materials. *Nat. Commun.* **2020**, *11*, No. 2229.
- (23) Song, Y.; Jin, S.; Kang, X.; Xiang, J.; Deng, H.; Yu, H.; Zhu, M. How a Single Electron Affects the Properties of the "Non-Superatom" Au<sub>25</sub> Nanoclusters. *Chem. Mater.* **2016**, *28*, 2609–2617.

- (24) Agrachev, M.; Ruzzi, M.; Venzo, A.; Maran, F. Nuclear and Electron Magnetic Resonance Spectroscopies of Atomically Precise Gold Nanoclusters. *Acc. Chem. Res.* **2019**, *52*, 44–52.
- (25) Li, Y.; Biswas, S.; Luo, T.-Y.; Juarez-Mosqueda, R.; Taylor, M. G.; Mpourmpakis, G.; Rosi, N. L.; Hendrich, M. P.; Jin, R. Doping Effect on the Magnetism of Thiolate-Capped 25-Atom Alloy Nanoclusters. *Chem. Mater.* **2020**, *32*, 9238–9244.
- (26) Li, Y.; Cowan, M. J.; Zhou, M.; Taylor, M. G.; Wang, H.; Song, Y.; Mpourmpakis, G.; Jin, R. Heterometal-Doped  $M_{23}$  (M = Au/Ag/Cd) Nanoclusters with Large Dipole Moments. *ACS Nano* **2020**, *14*, 6599–6606.
- (27) Li, Y.; Zhou, M.; Song, Y.; Higaki, T.; Wang, H.; Jin, R. Double-Helical Assembly of Heterodimeric Nanoclusters into Supercrystals. *Nature* **2021**, *594*, 380–384.
- (28) Kim, B.; Seong, H.; Song, J. T.; Kwak, K.; Song, H.; Tan, Y. C.; Park, G.; Lee, D.; Oh, J. Over a 15.9% Solar-to-CO Conversion from Dilute CO<sub>2</sub> Streams Catalyzed by Gold Nanoclusters Exhibiting a High CO<sub>2</sub> Binding Affinity. ACS Energy Lett. 2020, 5, 749–757.
- (29) Li, Y.; Li, S.; Nagarajan, A. V.; Liu, Z.; Nevins, S.; Song, Y.; Mpourmpakis, G.; Jin, R. Hydrogen Evolution Electrocatalyst Design: Turning Inert Gold into Active Catalyst by Atomically Precise Nanochemistry. *J. Am. Chem. Soc.* **2021**, *143*, 11102–11108.
- (30) Shichibu, Y.; Negishi, Y.; Watanabe, T.; Chaki, N. K.; Kawaguchi, H.; Tsukuda, T. Biicosahedral Gold Clusters  $[\mathrm{Au}_{25}(\mathrm{PPh}_3)_{10}(\mathrm{SC}_n\mathrm{H}_{2n+1})_5\mathrm{Cl}_2]^{2+}$  (n=2-18): A Stepping Stone to Cluster-Assembled Materials. J. Phys. Chem. C **2007**, 111, 7845–7847.
- (31) Jin, R.; Liu, C.; Zhao, S.; Das, A.; Xing, H.; Gayathri, C.; Xing, Y.; Rosi, N. L.; Gil, R. R.; Jin, R. Tri-Icosahedral Gold Nanocluster [Au<sub>37</sub>(PPh<sub>3</sub>)<sub>10</sub>(SC<sub>2</sub>H<sub>4</sub>Ph)<sub>10</sub>X<sub>2</sub>]<sup>+</sup>: Linear Assembly of Icosahedral Building Blocks. *ACS Nano* **2015**, *9*, 8530–8536.
- (32) Chiu, T.-H.; Liao, J.-H.; Gam, F.; Chantrenne, I.; Kahlal, S.; Saillard, J.-Y.; Liu, C. W. Homoleptic Platinum/Silver Superatoms Protected by Dithiolates: Linear Assemblies of Two and Three Centered Icosahedra Isolobal to Ne<sub>2</sub> and I<sub>3</sub><sup>-</sup>. *J. Am. Chem. Soc.* **2019**, 141, 12957–12961.
- (33) Yuan, S.-F.; Xu, C.-Q.; Liu, W.-D.; Zhang, J.-X.; Li, J.; Wang, Q.-M. Rod-Shaped Silver Supercluster Unveiling Strong Electron Coupling between Substituent Icosahedral Units. *J. Am. Chem. Soc.* **2021**, *143*, 12261–12267.
- (34) Li, Y.; Taylor, M. G.; Luo, T.-Y.; Song, Y.; Rosi, N. L.; Mpourmpakis, G.; Jin, R. Heteroatom Tracing Reveals the 30-Atom Au-Ag Bimetallic Nanocluster as a Dimeric Structure. *J. Phys. Chem. Lett.* **2020**, *11*, 7307–7312.
- (35) Zeng, C.; Chen, Y.; Iida, K.; Nobusada, K.; Kirschbaum, K.; Lambright, K. J.; Jin, R. Gold Quantum Boxes: On the Periodicities and the Quantum Confinement in the Au<sub>28</sub>, Au<sub>36</sub>, Au<sub>44</sub>, and Au<sub>52</sub> Magic Series. *J. Am. Chem. Soc.* **2016**, *138*, 3950–3953.
- (36) Takano, S.; Yamazoe, S.; Koyasu, K.; Tsukuda, T. Slow-Reduction Synthesis of a Thiolate-Protected One-Dimensional Gold Cluster Showing an Intense Near-Infrared Absorption. *J. Am. Chem. Soc.* 2015, 137, 7027–7030.
- (37) Xu, W. W.; Li, Y.; Gao, Y.; Zeng, X.-C. Unraveling a Generic Growth Pattern in Structure Evolution of Thiolate-Protected Gold Nanoclusters. *Nanoscale* **2016**, *8*, 7396–7401.
- (38) Shichibu, Y.; Konishi, K. Electronic Properties of [Core+exo]-Type Gold Clusters: Factors Affecting the Unique Optical Transitions. *Inorg. Chem.* **2013**, *52*, 6570–6575.
- (39) Katla, S. K.; Zhang, J.; Castro, E.; Bernal, R. A.; Li, X. Atomically Precise  $Au_{2S}(SG)_{18}$  Nanoclusters: Rapid Single-Step Synthesis and Application in Photothermal Therapy. *ACS Appl. Mater. Interfaces* **2018**, *10*, 75–82.
- (40) Jiang, X.; Du, B.; Huang, Y.; Yu, M.; Zheng, J. Cancer Photothermal Therapy with ICG-Conjugated Gold Nanoclusters. *Bioconjugate Chem.* **2020**, *31*, 1522–1528.
- (41) Yang, Y.; Zhou, Y.; Wang, S.; Wang, X.; Liu, X.; Xie, A.; Shen, Y.; Zhu, M. A Structurally Precise  $\operatorname{Ag}_x\operatorname{Au}_{25-x}$  Nanocluster Based Cancer Theranostic Platform with Tri-Targeting/in Situ O<sub>2</sub>-Generation/Aggregation Enhanced Fluorescence Imaging/Photo-

thermal-Photodynamic Therapies. *Chem. Commun.* **2020**, *56*, 9842–9845.

- (42) Gan, Z.; Lin, Y.; Luo, L.; Han, G.; Liu, W.; Liu, Z.; Yao, C.; Weng, L.; Liao, L.; Chen, J.; Liu, X.; Luo, Y.; Wang, C.; Wei, S.; Wu, Z. Fluorescent Gold Nanoclusters with Interlocked Staples and a Fully Thiolate-Bound Kernel. *Angew. Chem., Int. Ed.* **2016**, *55*, 11567–11571.
- (43) Qian, H.; Zhu, Y.; Jin, R. Size-Focusing Synthesis, Optical and Electrochemical Properties of Monodisperse Au<sub>38</sub>(SC<sub>2</sub>H<sub>4</sub>Ph)<sub>24</sub> Nanoclusters. *ACS Nano* **2009**, *3*, 3795–3803.
- (44) Das, A.; Li, T.; Li, G.; Nobusada, K.; Zeng, C.; Rosi, N. L.; Jin, R. Crystal Structure and Electronic Properties of a Thiolate-Protected Au<sub>24</sub> Nanocluster. *Nanoscale* **2014**, *6*, 6458–6462.
- (45) Dainese, T.; Antonello, S.; Bogialli, S.; Fei, W.; Venzo, A.; Maran, F. Gold Fusion: From Au<sub>25</sub>(SR)<sub>18</sub> to Au<sub>38</sub>(SR)<sub>24</sub>, the Most Unexpected Transformation of a Very Stable Nanocluster. *ACS Nano* **2018**, *12*, 7057–7066.
- (46) Ito, E.; Takano, S.; Nakamura, T.; Tsukuda, T. Controlled Dimerization and Bonding Scheme of Icosahedral M@Au<sub>12</sub> (M = Pd, Pt) Superatoms. *Angew. Chem., Int. Ed.* **2021**, *60*, 645–649.
- (47) Higaki, T.; Liu, C.; Zeng, C.; Jin, R.; Chen, Y.; Rosi, N. L.; Jin, R. Controlling the Atomic Structure of Au<sub>30</sub> Nanoclusters by a Ligand-Based Strategy. *Angew. Chem., Int. Ed.* **2016**, 55, 6694–6697.
- (48) Zhou, M.; Higaki, T.; Hu, G.; Sfeir, M. Y.; Chen, Y.; Jiang, D.; Jin, R. Three-Orders-of-Magnitude Variation of Carrier Lifetimes with Crystal Phase of Gold Nanoclusters. *Science* **2019**, *364*, 279–282.
- (49) Dickerson, E. B.; Dreaden, E. C.; Huang, X.; El-Sayed, I. H.; Chu, H.; Pushpanketh, S.; McDonald, J. F.; El-Sayed, M. A. Gold Nanorod Assisted Near-Infrared Plasmonic Photothermal Therapy (PPTT) of Squamous Cell Carcinoma in Mice. *Cancer Lett.* **2008**, 269, 57–66.
- (50) Pellegrino, T.; Manna, L.; Kudera, S.; Liedl, T.; Koktysh, D.; Rogach, A. L.; Keller, S.; Rädler, J.; Natile, G.; Parak, W. J. Hydrophobic Nanocrystals Coated with an Amphiphilic Polymer Shell: A General Route to Water Soluble Nanocrystals. *Nano Lett.* **2004**, *4*, 703–707.
- (51) Kim, S.-W.; Kim, S.; Tracy, J. B.; Jasanoff, A.; Bawendi, M. G. Phosphine Oxide Polymer for Water-Soluble Nanoparticles. *J. Am. Chem. Soc.* **2005**, 127, 4556–4557.
- (52) Negishi, Y.; Nobusada, K.; Tsukuda, T. Glutathione-Protected Gold Clusters Revisited: Bridging the Gap between Gold(I)-Thiolate Complexes and Thiolate-Protected Gold Nanocrystals. *J. Am. Chem. Soc.* 2005, 127, 5261–5270.
- (53) Zhou, M.; Jin, R.; Sfeir, M. Y.; Chen, Y.; Song, Y.; Jin, R. Electron Localization in Rod-Shaped Triicosahedral Gold Nanocluster. *Proc. Natl. Acad. Sci. U.S.A.* **2017**, *114*, E4697–E4705.
- (54) Aikens, C. M. Electronic and Geometric Structure, Optical Properties, and Excited State Behavior in Atomically Precise Thiolate-Stabilized Noble Metal Nanoclusters. *Acc. Chem. Res.* **2018**, *51*, 3065–3073.
- (55) Pei, Y.; Wang, P.; Ma, Z.; Xiong, L. Growth-Rule-Guided Structural Exploration of Thiolate-Protected Gold Nanoclusters. *Acc. Chem. Res.* **2019**, *52*, 23–33.
- (56) Li, Y.; Cowan, M. J.; Zhou, M.; Luo, T.-Y.; Song, Y.; Wang, H.; Rosi, N. L.; Mpourmpakis, G.; Jin, R. Atom-by-Atom Evolution of the Same Ligand-Protected Au<sub>21</sub>, Au<sub>22</sub>, Au<sub>22</sub>Cd<sub>1</sub>, and Au<sub>24</sub> Nanocluster Series. *J. Am. Chem. Soc.* **2020**, *142*, 20426–20433.

### ☐ Recommended by ACS

## Au Atoms Anchored on Amorphous $C_3N_4$ for Single-Site Raman Enhancement

Jian Yu, Lin Guo, et al.

NOVEMBER 23, 2022
JOURNAL OF THE AMERICAN CHEMICAL SOCIETY

READ 🗹

#### **Surfactant Layers on Gold Nanorods**

Jesús Mosquera, Luis M. Liz-Marzán, et al.

MAY 08, 2023

ACCOUNTS OF CHEMICAL RESEARCH

READ 🗹

## Tracking the Growth of Chiral Plasmonic Nanocrystals at Molybdenum Disulfide Heterostructural Interfaces

Jun Jiang Luo, Bang Lin Li, et al.

FEBRUARY 14, 2023

LANGMUIR

READ **C** 

### **Quantitative Analysis of the Shape Effect of Thermoplasmonics in Gold Nanostructures**

Huiming Zhang, Ming Li, et al.

APRIL 17, 2023

THE JOURNAL OF PHYSICAL CHEMISTRY LETTERS

READ 🗹

Get More Suggestions >